Pillars as antipinning centers in superconducting films

G. R. Berdiyorov,[1] V. R. Misko,[1] M. V. Milošević,[1,2] W. Escoffier,[3] I. V. Grigorieva,[3] and F. M. Peeters[1,*]
[1]*Departement Fysica, Universiteit Antwerpen, Groenenborgerlaan 171, B-2020 Antwerpen, Belgium*
[2]*Department of Physics, University of Bath, Claverton Down, Bath BA2 7AY, United Kingdom*
[3]*School of Physics and Astronomy, University of Manchester, Manchester M13 9PL, United Kingdom*
(Received 18 July 2007; revised manuscript received 26 November 2007; published 28 January 2008)

Using the nonlinear Ginzburg-Landau theory we study vortex configurations in a superconducting thin film with a square array of pillars in the presence of a uniform applied magnetic field. The presence of the pillars changes the vortex structures in the superconducting film considerably: a transition between triangular and square vortex lattices takes place with increasing size and/or height of the pillars and vortex lines and vortex clusters can be obtained for particular applied magnetic fields. All of these findings are summarized into an equilibrium vortex phase diagram, which shows the transition between different ground-state vortex configurations as a function of the radius and periodicity of pillars. For larger radius of the pillars vortices start to penetrate the pillars and order in vortex shell structures both inside and around the pillars. The theoretical results are complemented by an experimental study of the vortex configurations in single-crystal based Nb pillars with radius $R \sim 0.5-2$ μm. Using Bitter decoration, concentric shells of vortices are revealed inside the pillars and shell-like structures are found at the interstitial sites, in accordance with the theoretical results. In addition, the observed distortion of the vortex shell structures by weak pinning centers present in our Nb samples is investigated by molecular dynamics simulations. We also show that the transition between predicted vortex states can be obtained from the temperature dependence of local magnetization measurements.

DOI: 10.1103/PhysRevB.77.024526 PACS number(s): 74.20.De, 74.25.Dw, 74.78.Na, 74.25.Ha

I. INTRODUCTION

Superconducting systems with periodic arrays of artificial pinning centers have received much attention over the past decade, mostly with the aim to increase the critical parameters of the superconductors. Most interest has been focused on regular arrays of holes (antidots),[1–4] blind holes,[5,6] and magnetic dots.[7,8] Superconducting vortices in the presence of periodic arrays of pinning centers reveal a wide range of interesting commensurability and matching effects when the number of vortices is a multiple or rational multiple of the number of pinning sites. These highly ordered vortex configurations lead to a strong enhancement of the critical current. However, real-world superconducting materials, especially high temperature superconductors, which are fabricated through a complex synthesis route, have structural defects at many length scales and in a wide variety of shapes leading to complex static and dynamic processes. Therefore, it becomes of particular interest to model this complex family of defects in a way that allows one to optimize the critical parameters for a given superconducting material. Given such complexity, it is desirable to reduce the problem to a quantitative study of the effectiveness of specific types of defects. With this knowledge, it then becomes clear how to either progressively combine them to establish their collective effectiveness or isolate the best pinning sites and remove the others.

The aim of the present work is to study the stable vortex structures in thin superconducting films with arrays of pillars, which can be viewed as the inverse type of defects to a lattice of antidots or blind holes. In the latter case, antidots (blind holes) are used to pin vortices, whereas in our sample individual pillars repel vortices and thus serve as "antipinning" sites. As a consequence, the interaction of flux lines with arrays of pillars is substantially different from the more widely investigated vortex-antidot or vortex-blind hole interactions. However, we find that the results obtained with the present system can be related to superconducting films with arrays of antidots or blind holes beyond the pinning-site-saturation field (i.e., maximal number of pinned vortices is reached), where the additional vortices are repelled by the pinned ones in the holes. A superconducting film with arrays of out-of-plane magnetized magnetic dots also presents a system similar to our sample, when the applied field is antiparallel to the magnetic moment of the dots (see, for example, Ref. 8). In the latter case vortices are repelled from the magnetic dot area due to the encircling supercurrent of the same chirality induced by the stray field of the magnetic dots.

The problem of the vortex-pillar interaction was studied in Ref. 5 within the linearized Ginzburg-Landau (GL) theory in the case of a *single* pillar on top of a superconducting film. It was shown that the gradual change from a blind hole into a disk of the same radius which rests on top of the film (i.e., with increasing bottom thickness of the blind hole) is accompanied by an abrupt decrease in the number of vortices inside the blind hole area. Here, we extend this work to a *lattice of pillars* and we solve the two coupled nonlinear GL equations, where demagnetization effects are fully taken into account.

The latest advances in lithographic techniques based on modern electron-beam and etching procedures allow one to design superconducting films with a large array of pillars of different shapes and sizes. These systems enable one not only to study possible vortex configurations, but also to get enough statistics to identify stable and metastable configurations of interacting vortices and consider the effect of the sample geometry on the final vortex state.[9,10]

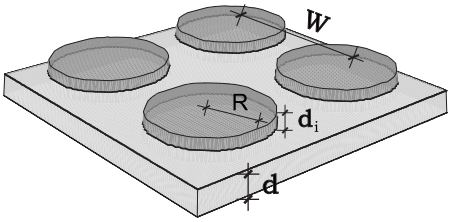

FIG. 1. Schematic view of the sample: a superconducting film (thickness d) with a regular array (period W) of pillars with radius R and thickness d_i.

In this work, we consider a superconducting film with an array of superconducting pillars. We find that for smaller size of the pillars vortices form somewhat deformed triangular lattice structures, where the force of vortex-vortex interaction overcomes the repulsive force exerted by the pillars. For larger pillars vortices become "pinned" between the pillars due to the "caging" effect. Different ordered vortex lattice structures are obtained for larger density of vortices with possible shell structures and we examine in detail the effect of the pillar size on the flux-line pattern formation. Furthermore, we study the effect of weak disorder on the vortex patterns in and around the pillars and compare the results with experiment where vortex structures in Nb samples with arrays of pillars were visualized directly using Bitter decoration.

The paper is organized as follows. The details of our theoretical formalism are given in Sec. II. We consider a superconducting film with small-diameter pillars in Sec. III, where we focus on the vortex patterns at the interstitial sites. Section IV deals with larger pillars and we investigate vortex configurations both inside and between the pillars. The results of our Bitter decoration experiments for flux-line distributions inside and around single-crystal based Nb pillars are given in Sec. V, together with molecular dynamics simulations demonstrating the effect of weak pinning on the vortex patterns. All the findings are summarized in Sec. VI.

II. THEORETICAL FORMALISM

We consider a superconducting film (of thickness d) with a square array of pillars (of radius R, period W, and thickness $d_i > d$) in the presence of a perpendicular uniform magnetic field (see Fig. 1). For the given system we solved two nonlinear GL equations, which can be written in dimensionless units in the following form [assuming d, $d_i < \xi(T)$]:[11]

$$(-i\nabla - \mathbf{A})^2\Psi = \Psi(1 - |\Psi|^2) + i(-i\nabla - \mathbf{A})\Psi\frac{\nabla d(x,y)}{d(x,y)}, \tag{1}$$

$$-\Delta\mathbf{A} = \frac{d(x,y)\xi}{\lambda^2}\delta(z)\mathbf{j}, \tag{2}$$

where

$$\mathbf{j} = \frac{1}{2i}(\Psi^*\nabla\Psi - \Psi\nabla\Psi^*) - |\Psi|^2\mathbf{A} \tag{3}$$

is the local supercurrent density. The last term in Eq. (1) describes the effect of the variation of the sample thickness on the superconducting condensate. Equations (1) and (2) are solved using the iterative procedure as outlined in Ref. 12 in combination with the link-variable approach.[13] The magnitude of the applied magnetic field $H = n\Phi_0/S = H_n$ is determined by the number n of flux quanta $\Phi_0 = hc/2e = 2.07 \times 10^{-7}$ G cm^2 piercing through the simulation region area S. Our simulation region is a $W_s \times W_s$ square, with $W_s = 4W$, where W is the period of the lattice of pillars (i.e., 4×4 unit cells). The periodic boundary conditions for $\mathbf{A}$ and Ψ around the square simulation region are[14]

$$\mathbf{A}(\mathbf{r} + \mathbf{b}_i) = \mathbf{A}(\mathbf{r}) + \nabla\eta_i(\mathbf{r}), \tag{4}$$

$$\Psi(\mathbf{r} + \mathbf{b}_i) = \Psi\exp(2\pi i\eta_i(\mathbf{r})/\Phi_0), \tag{5}$$

where $\mathbf{b}_i$ $(i = x, y)$ is a translational lattice vector, and η_i is the gauge potential for the external vector potential (in our case Landau gauge, $\eta_x = HW_s y$, $\eta_y = 0$). The ground-state vortex configurations for a given magnetic field are determined by comparing the free energy of all stable vortex states found when starting from different randomly generated initial conditions [for initial $\psi(x,y) \approx 0$, such method corresponds to "field-cooled" experiments]. The dimensionless Gibbs free energy is calculated as

$$F = V^{-1}\int_V \left[2(\mathbf{A} - \mathbf{A}_0)\mathbf{j} - |\Psi|^4 + i(-i\nabla - \mathbf{A})\Psi\frac{\nabla d(x,y)}{d(x,y)}\right]d(x,y)dxdy, \tag{6}$$

where integration is performed over the volume V of the simulations region, and $\mathbf{A}_0$ is the vector potential of the applied uniform magnetic field. In this paper we present our results obtained for extreme type-II superconductors, i.e., $\kappa \gg 1$.

III. SMALL-RADIUS DISKS: INTERSTITIAL VORTEX STRUCTURES

Let us first consider a superconducting film with pillars of small size, into which vortex cannot penetrate. Figure 2 shows the ground-state vortex phase diagrams in the R-W plane for four matching fields and for two different values of the pillar thickness. Insets show Cooper-pair density plots of the corresponding states. As in the case of antidot arrays,[4] the structure of vortices depends not only on the radius of the pillars R but also on W, i.e., the proximity of the neighboring pillars in the lattice. At the first matching field [Fig. 2(a)] (i.e., one vortex per unit cell) and for small radius of the pillars, vortices form a slightly distorted triangular lattice due to the repulsive vortex-vortex interaction (inset 1). By increasing the radius of the pillars, or consequently by decreasing the interpillar distance W, vortices transit from the triangular lattice to the square one (inset 2), i.e., the same

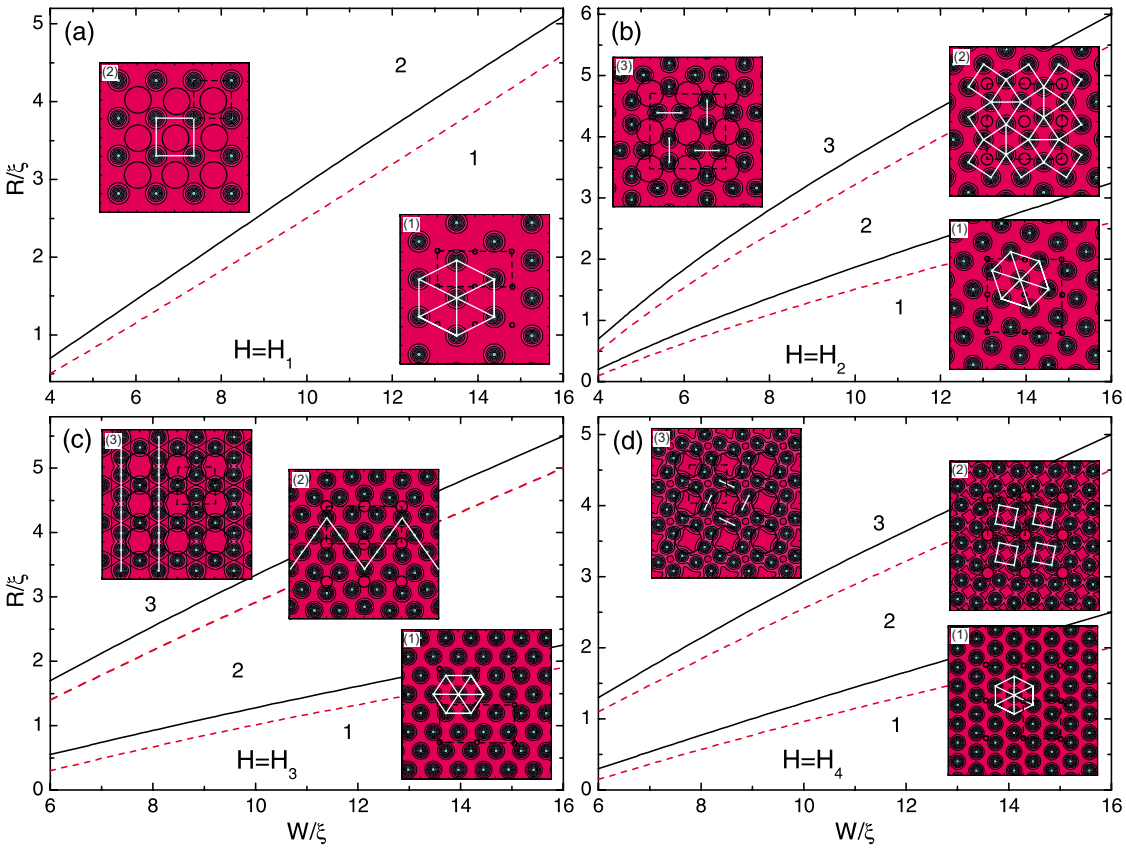

FIG. 2. (Color online) The thermodynamic equilibrium phase diagrams at the matching fields $H=H_1$ (a), $H=H_2$ (b), $H=H_3$ (c), and $H=H_4$ (d), as a function of the radius (R) and period (W) of the pillars. Solid (dashed) curves show the results for thickness of the pillars $d_i=0.1\xi$ ($d_i=0.4\xi$). The insets are contourplots of the Cooper-pair density of the corresponding states: magenta (dark gray) and/or cyan (light gray) regions indicate high and/or low density. The positions of the pillars are indicated by black circles and the vortex patterns are highlighted by the white lines. Black dashed lines show the unit cell for the overall vortex lattice.

translationally symmetric state as the pillar array. This means that large pillars form an effective pinning potential for vortices at the interstitial sites. Thus vortices are loosely "caged" at the interstitial positions. However, this pinning is much weaker than the pinning potential of antidots. Similar vortex configurations were obtained in a superconducting film containing an array of magnetic dots with out-of-plane magnetization in the case when the applied magnetic field is antiparallel to the magnetic moment of the dots.[7] These vortex states lead to weak matching features in the magnetization and critical current of the sample.

The ordering of the interstitial flux lines at the second matching field with increasing pillar size is the following [Fig. 2(b)]. Initially vortices form a deformed triangular lattice (inset 1) in order to minimize their mutual interaction. With increasing the size of the pillars vortices rearrange themselves and form the Delaunay triangulation for some radius of the pillars (inset 2). Finally, for larger sizes of the pillars, we obtain a state where two vortices are caged between the pillars and they alternate in position from one interstitial site to another (inset 3). The latter is the same structure in superconducting films with arrays of antidots with two interstitial vortices after the saturation of the antidots.[1]

The ground-state R-W phase diagram at the third matching field is shown in Fig. 2(c), which also represents ordered flux-line structures. For example, zigzag vortex chains are found for intermediate sizes of the pillars (inset 2) and these chains straighten along the y axis for larger radius R (inset 3). These kinds of parallel rows of vortices have been recently found experimentally in superconducting films but with elliptic pinning centers.[15]

When the size of the pillars is small, vortices form an almost perfect hexagonal lattice at the fourth matching field [inset 1 of Fig. 2(d)] because the elastic force of the vortex lattice overcomes the force arising from the square array of pillars. With increasing the radius of the pillars, vortices rearrange themselves at interstitial sites into trapped vortex molecules. Namely, vortex clusters containing four vortices and repeating periodically in space in a square lattice start forming in between the pillars for a larger radius of the pillars (inset 2). With further increase of R, the further compression of vortices is accommodated by a perfect alignment of the vortex molecules around the pillars and at the interstitial sites (inset 3).

The thickness of the pillars d_i also plays an important role in the final vortex structure in the sample. For example, with increasing d_i the critical pillar radius (for a given period W) for the transition between any two different vortex configurations decreases (see dashed curves in Fig. 2). The latter is due to the stronger repulsion of vortices from the pillars.

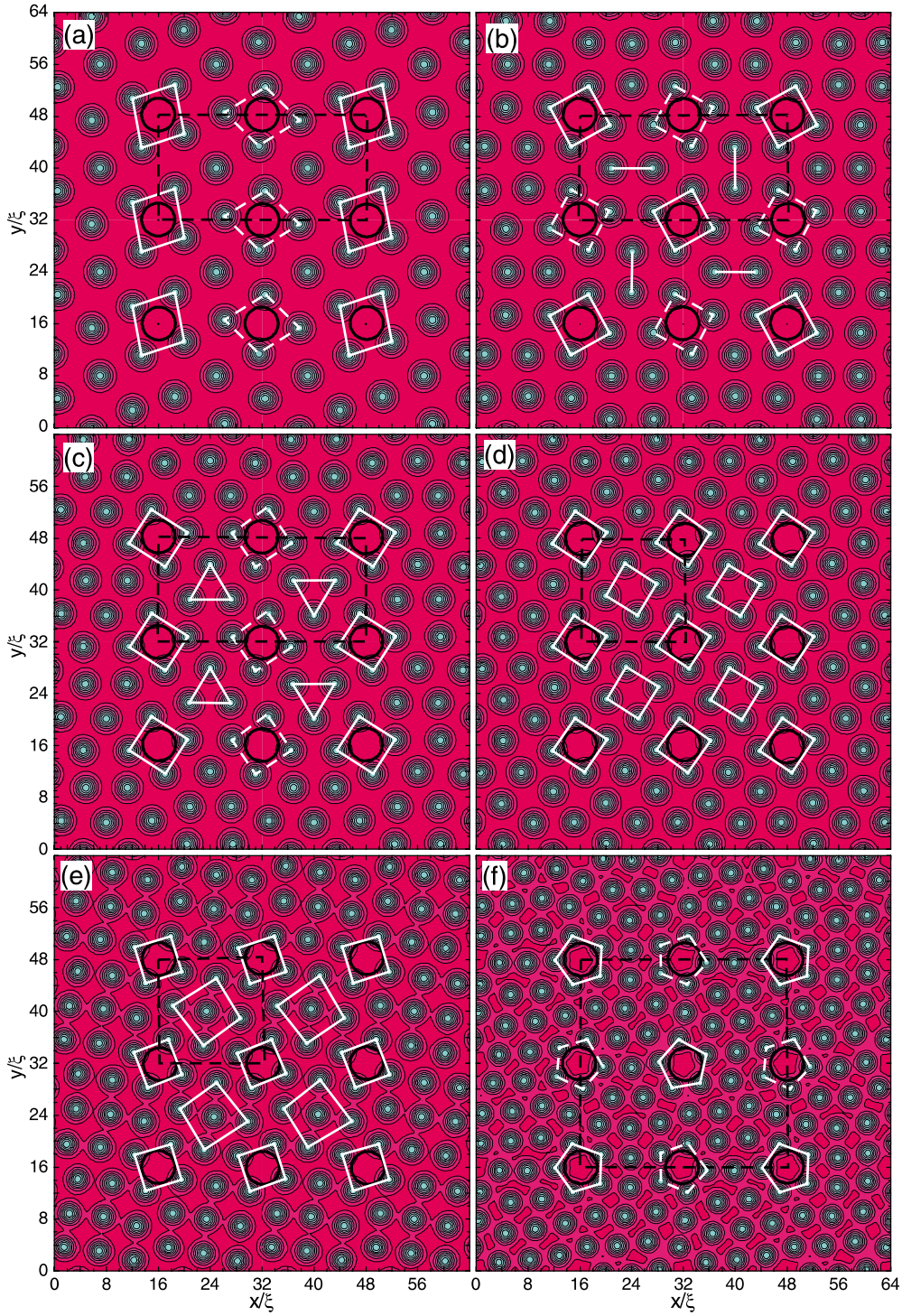

FIG. 3. (Color online) The ground-state vortex configurations for the applied fields $H=H_5-H_9$ [(a)–(e)] and $H=H_{12}$ (f). The period is $W=16\xi$, the radius $R=3\xi$, the pillars' thickness is $d_i=0.1\xi$, and the film thickness is $d=0.1\xi$.

In order to see the effect of the flux-line density on the ground-state vortex configurations in the present system, we conducted our calculations for larger applied fields. Figure 3 shows vortex structures obtained for the period $W=16\xi$ and the radius $R=3\xi$ of the pillars at higher magnetic fields. At the fifth matching field [Fig. 3(a)] vortices form a distorted triangular lattice avoiding the pillars. This state can also be viewed in a different way: four vortices form a cluster around the pillars and the fifth one is located in the center of the interstitial sites, i.e., it is now caged between the clusters. The orientation of clusters differs from one column to another (solid and dashed white lines in the figure). At $H=H_6$ [Fig. 3(b)] two vortices are located between the clusters of four vortices, which now change the orientation from one site to another. These alternating in position pairs of caged vortices show the structure obtained numerically[4] and also

observed experimentally[1] in superconducting films with arrays of antidots for two interstitial vortices. At $H=H_7$ [Fig. 3(c)] three "interstitial" vortices are oriented in a way that minimizes the free energy of the system. Clusters of four vortices with the same orientation are formed both at the interstitials and around the pillars for $H=H_8$ [Fig. 3(d)], i.e., a square lattice (rotated 45° with respect to the array of pillars) of clusters is formed. One additional vortex at $H=H_9$ comes to the middle of the interstitial site and has four closest neighbors [Fig. 3(e)]. With further increasing the applied field the triangular lattice of vortices (distorted close to the pillars) regains dominance [see Fig. 3(f)] and vortices start penetrating the pillars, which we will discuss in the following section.

The above predicted vortex structures can be observed using direct imaging techniques such as Bitter decoration[9] (see Sec. V). However, it becomes difficult to obtain clear images of vortices for larger density of vortices or for temperatures close to the critical one, where vortex cores start to overlap. In this respect, we suggest here another method which is based on the local magnetization measurements, i.e., Hall probe microcopy[16] measurements.

We consider a 20 nm thick Pb film with coherence length $\xi_0=40$ nm and the penetration depth $\lambda_0=42$ nm in the presence of a square array of pillars. The temperature dependence is included in the calculations as $\xi(T)=\xi_0/\sqrt{1-T/T_{c0}}$ and $\lambda(T)=\lambda_0/\sqrt{1-T/T_{c0}}$. Figure 4 shows the temperature dependence of magnetization (in units of H_{c2}) of the sample calculated over a $S=400\times400$ nm^2 area directly above the chosen interstitial site ($4\pi M=\langle h\rangle-H$) for the temperature sweep up (solid curves) and sweep down (dashed curves). It is seen from this figure that the magnetization in general decreases with increasing temperature as the average field inside the sample becomes equal to the applied one close to the critical temperature. In the case of larger pillars (blue solid and yellow dashed curves) the vortex structure does not change with temperature and vortices form a square lattice (see panels 1 and 2). The magnetization has paraboliclike dependence on temperature, which is different from the temperature dependence of the magnetization of bulk superconductors. In the latter case a linear $M(T)$ curve is obtained close to the critical temperature. In the case of smaller pillars we have initially a triangular lattice of vortices (see panel 3) and the transition to a square lattice takes place with increasing temperature (panel 4). During this transition magnetization increases, because the vortex comes exactly under the Hall probe. After the transition point M decreases again, thus we obtain a minimum in the magnetization curve. The position of the minimum shifts toward low temperatures as we increase the pillar size (compare black and red curves in the figure), which is due to the fact that the larger pillars generate stronger pinning for vortices at the interstitial sites. Such kinds of kinks in the temperature dependence of the magnetization are usually obtained, e.g., in studies of high-T_c superconductors (see, for example, Ref. 17), where the system undergoes first-and/or second-order phase transitions between different vortex states.

Magnetic hysteresis is routinely observed in superconductors and usually attributed to edge barriers (including both Bean-Livingston and geometric barriers) or to impurities and defects as pinning centers. Pillars in our case also create pinning centers (at the interstitial sites) for the vortices and this should be attributed in the magnetization loops of the sample. Therefore, we calculated the magnetization of our sample decreasing the temperature starting from the critical one, which is shown by dashed curves in the main panel of Fig. 4. In the case of larger pillars, where the vortex structure does not change with temperature (panels 1 and 2), no hysteresis is obtained and magnetization curves coincide with each other (blue solid and yellow dashed curves). A clear hysteresis in the magnetization loop appears for smaller size of pillars (solid and dashed red curves) and this hysteresis vanishes at temperatures close to T_c. Instead of the kink, a clear jump appears in the magnetization curve during the cooling. The height of the magnetization jump depends on the pillars size and vanishes with decreasing R (dashed black

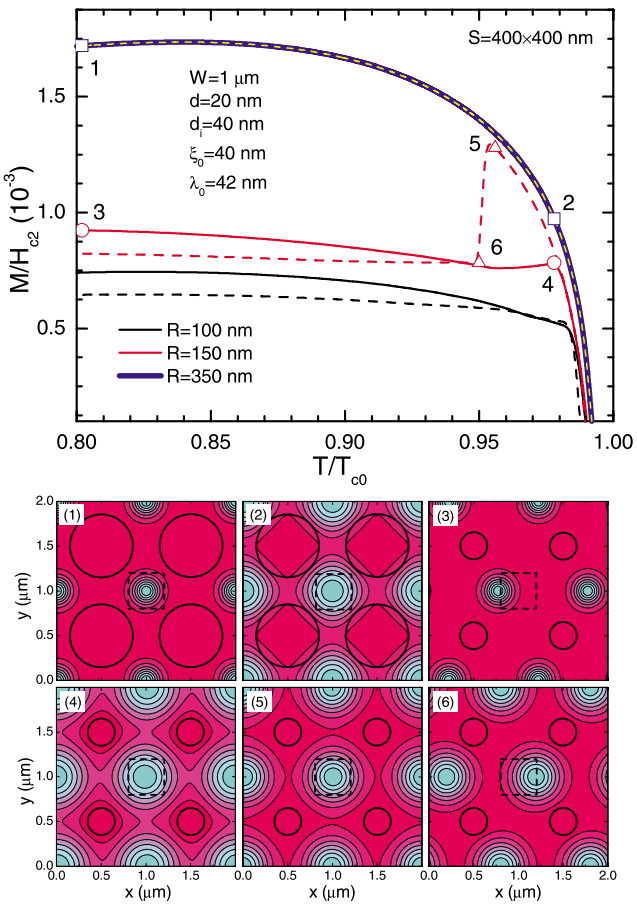

FIG. 4. (Color online) Magnetization as a function of temperature for pillar radii $R=100$ nm (black curves), $R=150$ nm (red curves), and $R=350$ nm (blue and yellow curves). Solid curves correspond to the temperature sweep up and dashed curves correspond to the temperature sweep down. Panels (1)–(6) show the Cooper-pair density plots of the vortex states at the temperatures indicated by open symbols in the main panel. The period of pillars is $W=1$ μm, the thickness of the pillars and the films is $d_i=d=20$ nm, the coherence length is $\xi_0=40$ nm, and the penetration depth is $\lambda=42$ nm. The magnetization is calculated over $S=400\times400$ nm^2 area above the interstitial site [dashed squares in panels (1)–(6)].

curve). This jump corresponds to the transition between different vortex states, i.e., from the square lattice of vortices to the triangular one (see panels 5 and 6). Therefore, the $M(T)$ behavior of the sample can be used as an indication of the transition between different vortex states predicted in this paper.

IV. LARGER RADIUS PILLARS: VORTEX SHELL STRUCTURES

Recent Bitter decoration experiments on superconducting samples with arrays of pillars[10] have shown that for larger spacing between the pillars, the vortex structure inside them is very similar to the one in individual superconducting disks. In addition, vortex configurations were found to be independent of the disk's height. Independent vortex structures have also been observed in superconducting films with arrays of blind holes, when the distance between the blind holes is much larger than their size.[5] However, when the pillars (or blind holes) are closely located, vortices in different pillars start to interact with each other through the interstitial vortices (or directly in the case of blind holes[18]) leading to the ordering of vortices in different pillars with respect to each other. Thus vortex structures in adjacent pillars cannot be considered as independent.

In this section we investigate the vortex structures inside the pillars for small interpillar distances, thus taking into account the influence of interstitial vortices on the final vortex state. The results will be compared to the ones obtained earlier for individual thin film disks.[9,20–22] In the latter system vortices form well-defined "concentric" shell structures, while filling these shells according to specific rules (the so-called "magic numbers"). As a result, a "Periodic Table" for the shell formation can be constructed, similarly to electron shells in atoms. For larger radius of the disks vortex-vortex interaction starts to dominate over the confinement imposed by the boundary, and the Abrikosov vortex lattice is restored in the center of the disks.[23]

Before considering vortex distribution inside the pillars, let us first discuss the problem of surface barrier for the vortex entry and exit in the case of superconducting pillars. This barrier, also called Bean-Livingston energy barrier, is always present in finite size superconductors and leads to strong hysteretic effects and different vortex phase transitions.[25] We considered a superconducting disk with radius R and thickness d_i on top of another superconductor with radius $R_0=2R$ and thickness d and follow the approach given in Ref. 24 to calculate the surface barrier. The results for $R=4\xi$ and $d_i+d=0.5\xi$ are given in Fig. 5, which shows the free energy of the system as a function of the radial position of the vortex. For $d=0$ ($d_i=0.5\xi$), i.e., just a superconducting disk with radius $R=4\xi$, there is a barrier both for vortex penetration and expulsion (solid curve). If we add a thin layer of a superconducting material at the bottom of the disk (dashed curve) both the penetration and the expulsion barriers for the vortex in the pillar increase, whereas there is virtually no energy barrier for the vortex to leave the big disk. With further increasing d, a double minimum appears in the free energy, one corresponding to the vortex sitting in the center of the pillar and the other one for the vortex positioned in the bottom disk (dash-dotted curve). By further increasing d our system becomes a plain disk with radius R_0 and for the chosen value of the magnetic field there is no barrier for the vortex to enter our system. Nevertheless, shown presence of the energy barrier for the vortex at the pillar-bottom disk interface implies that once entered inside the pillars, vortices can form ordered structures there, almost as if they were individual disks (see Ref. 9).

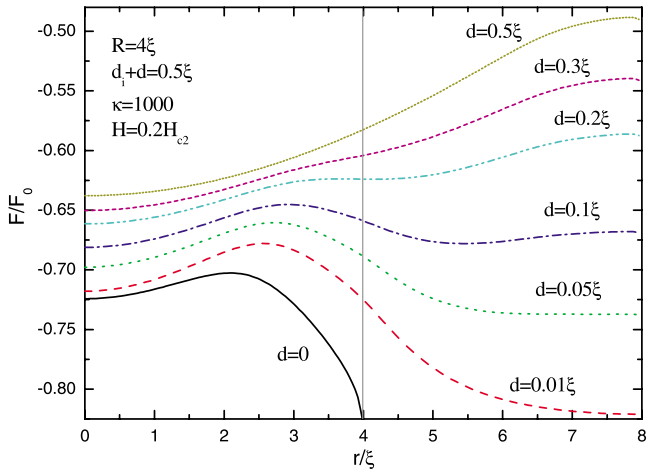

FIG. 5. (Color online) The free energy as a function of the radial position of the vortex in a superconducting disk with radius $R=4\xi$ (thickness d_i) on top of another disk of radius $R_0=8\xi$ (thickness d).

Figure 6 shows the vortex structure in the superconducting film with arrays of pillars of radius $R=5\xi$ and period $W=12\xi$ for different applied fields. As in the case of mesoscopic superconductors, we use the notation L for the number of vortices inside the pillars. Thus, this figure shows the evolution of vortices inside the pillars for vorticity up to $L=7$. Note that in periodically arranged pillars with close spacing, vortex structures in the different pillars cannot have an arbitrary orientation, and they are interlocked with the specific position of the interstitial vortices, as discussed in following paragraphs.

For $L=2$, vortices form dimers and they are tilted by $\pi/2$ from one pillar to another [see white lines in Fig. 6(a)]. Similar alignment of dimers was also obtained for vortices in blind hole arrays.[18] Contrary to the blind hole case the orientational ordering of vortices in the pillars is due to the structure of vortices outside the pillars, which changes from one interstitial site to another (the white dashed squares in the figure). A ferromagneticlike alignment of the dimers can also be obtained for some chosen specific magnetic fields. In the same manner as the dimers, the trimers are also orientationally ordered pointing up and down in different rows of pillars [Fig. 6(c)]. In Fig. 6(d) all trimers point into the same direction in spite of different vortex structures at adjacent interstitial sites. With increasing the applied magnetic field each pillar captures four vortices which form a square and they are all aligned for $H=H_{12}$, as shown in Fig. 6(e). This type of n-mer ordering is similar to the colloidal molecular crystals on a periodic substrate,[19] with the difference that in our case vortices interact through the interstitial vortices.

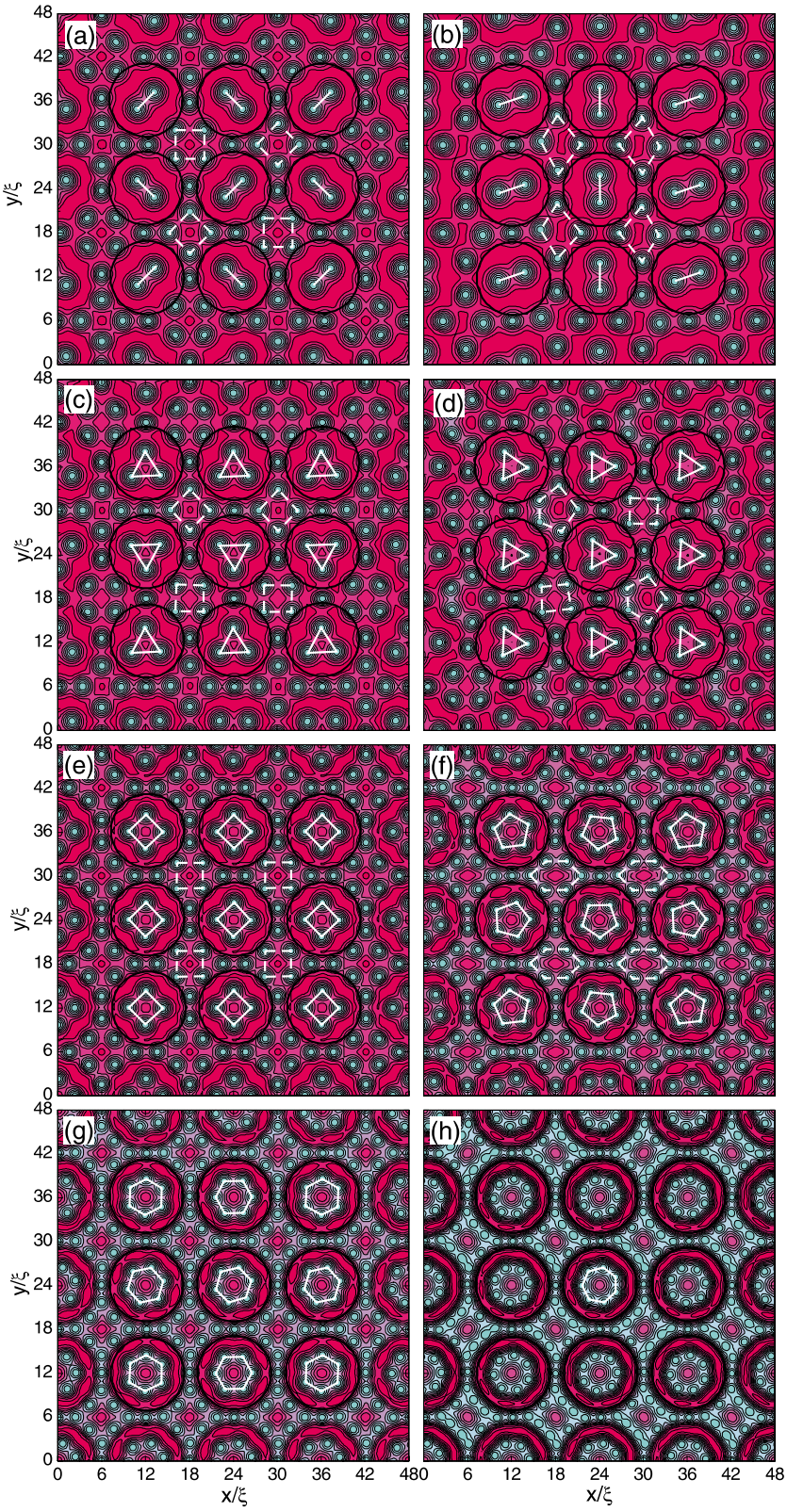

FIG. 6. (Color online) The vortex structure in the applied magnetic field $H=H_8$ (a), $H=H_{6.5}$ (b), $H=H_9$ (c), $H=H_{9.5}$ (d), $H=H_{12}$ (e), $H=H_{14}$ (f), $H=H_{16}$ (g), and $H=H_{19}$ (h). The radius of the disks (indicated by black circles) is $R=5\xi$, the period $W=12\xi$, the film thickness is $d=0.1\xi$, and the thickness of the pillars is $d_i=0.1\xi$. The white dashed lines indicate the vortex lattice structure inside the pillars (at the interstitials).

However, the latter can also change the confinement to the pinned vortices, leading to nonsymmetric and thus much richer and more complex vortex structures.

Let us now have a closer look at the vortex state formation process inside individual pillars. Although different stable vortex configurations can be obtained for fixed L, we restricted ourselves only to the ground-state vortex configurations. As shown in Figs. 6(a)–6(f) the effect of vortex confinement in the pillars up to $L=5$ is very similar to that found previously in individual disks,[9,20–22] i.e., vortices are located in a single shell and form regular polygons (see also Ref. 26). However, the first shell in our case can contain up to

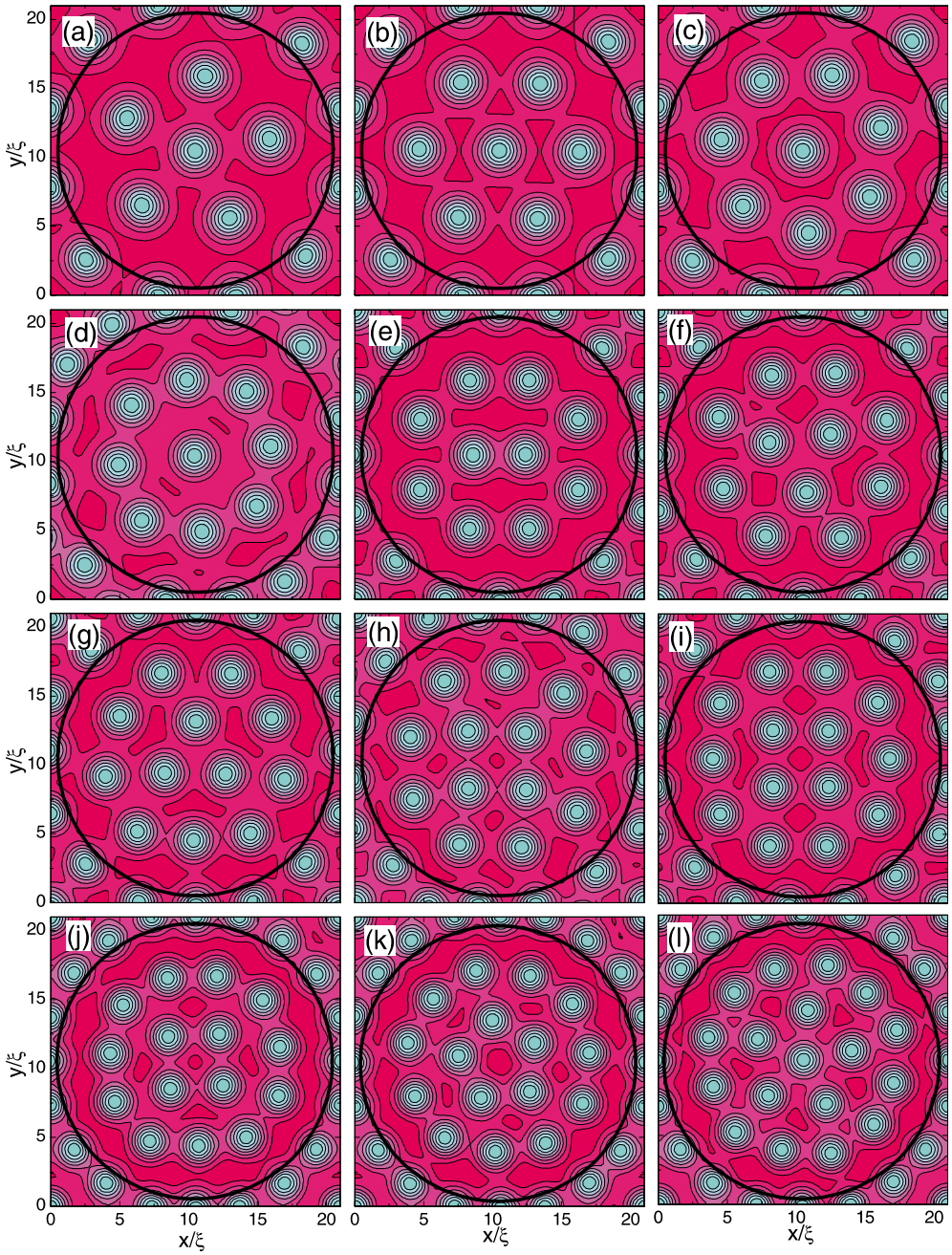

FIG. 7. (Color online) The vortex structure inside the pillars of radius $R=10\xi$ and period $W=21\xi$ for the number of pinned vortices $L=6-16$ [(a)–(k)] and $L=18$ (l). The film thickness is $d=0.1\xi$ and the thickness of the pillars is $d_i=0.1\xi$.

seven vortices [Fig. 6(h)], whereas in finite size superconductors the second shell of vortices already starts to form at $L=6$ with a single vortex in the center of the disk and five vortices around it. In the same manner the (1,6) state is obtained for $L=7$.

A recent theoretical analysis[22] showed that the vortex configurations in individual superconducting disks are not universal and do depend on the size and thickness of the superconducting disks. For example, earlier theoretically predicted,[21,26] but not observed experimentally,[9] the (1,8) state for $L=9$ is stable only for small-size disks and it transits to the (2,7) state for larger size and thicker disks.

In order to see the effect of the pillar size on the vortex pattern formation we conducted our calculations for the arrays of pillars of radius $R=10\xi$ and period $W=21\xi$. Figure 7 shows the distribution of vortices inside the pillars (restricted to a single unit cell) for the number of vortices ranging from $L=6$ to $L=16$ and for the $L=18$ state. The evolution of vortex shells in the pillars in this case is as follows: for $L\leqslant 5$ all the vortices are arranged in a single shell, as was found for small-radius pillars [see Figs. 6(a)–6(f)]. The formation of a second shell starts from $L=6$ with one vortex in the center and five others in the second shell [Fig. 7(a)]. The next three vortices are added to the outer shell and we have the states (1,6), (1,7), and (1,8) [see Figs. 7(b)–7(d)]. The state with two vortices in the center and others in the outer shell exists only for the $L=10$ state [Fig. 7(e)] and with further increasing the number of vortices the inner shell starts to grow. The maximum number of vortices in the inner shell is 5, which is reached for $L=16$ state [Fig. 7(k)]. The formation of a third

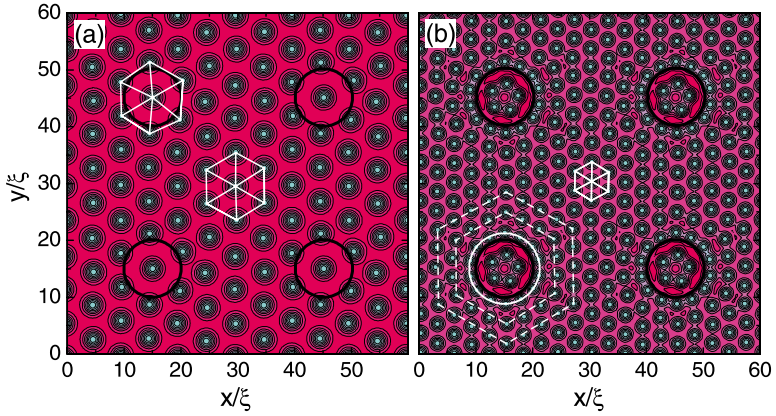

FIG. 8. (Color online) The vortex structure in a superconducting film with an array of pillars of radius $R=5\xi$ and lattice size $W=30\xi$ for the applied fields $H=H_{30}$ (a) and $H=H_{90}$ (b).

shell starts at $L=18$ with one vortex in the center, surrounded by a ring of 5 vortices, which is surrounded by a larger ring of 12 vortices [Fig. 7(l)]. With further increasing the applied magnetic field giant-vortex states are formed; individual vortices are compressed into centered multiquanta (giant) vortex, and superconductivity survives only at the edges of the pillars. For this radius and period of the pillars vortices form structures identical to those obtained for individual finite size superconducting disks, except for the $L=9$ and $L=17$ states. In the former case we obtain the (1,8) state, while in the experiment[9] the (2,7) state was found to be stable, and in the latter case we have two shells of vortices [(6,11) state], while earlier theoretical works predicted the (1,5,11) state.[20,22]

Next we investigate the influence of larger-size pillars on the structure of interstitial vortices. Figures 8(a) and 8(b) show the vortex distribution in the sample for the radius of pillars $R=5\xi$ for two different values of the applied field. For small applied field only one vortex is pinned by the pillars and the entire vortex lattice is triangular [Fig. 8(a)]. With increasing applied field a vortex ring is formed *around the pillar* [white circle in Fig. 8(b)], i.e., the pillar imposes its symmetry on the vortex structure. However, the effect of the pillars on the vortex configuration dies away in the middle region between the disks where transition from the vortex ring structure to a triangular vortex lattice takes place. Due to the interplay between the vortex shells around the pillars and the triangular lattice deep in the intermediate region, vortices form hexagonlike line structures [dashed white lines in Fig. 8(b)] around the pillars.

From the above figure it is not clear if the boundary of the pillars or the vortex structure inside the pillars has a stronger effect on the interstitial vortices. To bring more understanding to this issue, we performed calculations for different thicknesses of the pillars, starting from the blind hole case up to the limiting case of our approach, i.e., $d_i+d=\xi$. Figure 9 shows the vortex structure for different heights of the pillars: $d_i=0.5\xi$ [(a) and (b)], $d_i=0.2\xi$ [(c) and (d)], and $d_i=0.01\xi$ [(e) and (f)], and for $R=10\xi$. The film thickness is $d=0.1\xi$ and the period of the pillars is $W=30\xi$. In spite of the fact that only two vortices are located inside the pillars at small applied fields, two clear shells of interstitial vortices are found around the pillars [Fig. 9(a)], which is in this case due to the circular geometry and larger thickness of the pillars. The number of shells around the disks increases up to 4 for larger fields [Fig. 9(b)]. If we decrease the thickness of the pillars (keeping the number and structure of vortices inside the pillars similar) the number of vortex shells around the pillars decreases [see Figs. 9(c) and 9(d)]. If we further suppress the pillars' thickness, the pillars turn into blind holes and, consequently, the number of pinned vortices considerably increases [Figs. 9(e) and 9(f)]. In this case vortex ring structures in the interstitials are still present, although only pinned vortices interact repulsively with the interstitial ones, i.e., the effect of the blind hole edges is less relevant to our study. This indicates that while the geometry of pillars imposes its geometry on trapped vortices, vortex-vortex interaction plays essential role in the formation of shell structures at the interstitial sites. However, pillar height is still important for the number of surrounding vortex shells, as it regulates the amplitude of the current within it, and consequent span of the pillars antipinning potential for interstitial vortices. Note that in the case of blind holes each hole is surrounded by a region which is practically free of vortices (due to large encircling screening currents), while in the case of pillars vortices are closely located to the edge of the pillars (due to the strong intervortex repulsion at interstitials).

V. BITTER DECORATION EXPERIMENTS

A. Vortex shells in the presence of disorder

In the previous sections we showed that vortices form ordered lattice structures in superconducting films with regular arrays of pillars. It was also shown that depending on the density of the vortices and on the dimensions of the pillars, concentric vortex shells can be obtained around the pillars. These highly ordered vortex configurations could be directly observed using, e.g., Lorenz microscopy,[1] because at low enough temperatures vortices are well separated and have a very high magnetic contrast. Vortex distributions in nanostructured superconductors can also be visualized by the Bitter decoration technique. Very recently, Bitter decoration experiments showed the formation of vortex shells[9] and clusters[10] in freestanding small Nb disks.

In this section we compare some of the predicted vortex configurations for sparse arrays of pillars ($W \gg R$) with those observed experimentally in single-crystalline Nb platelets with comparable square arrays of circular pillars etched in

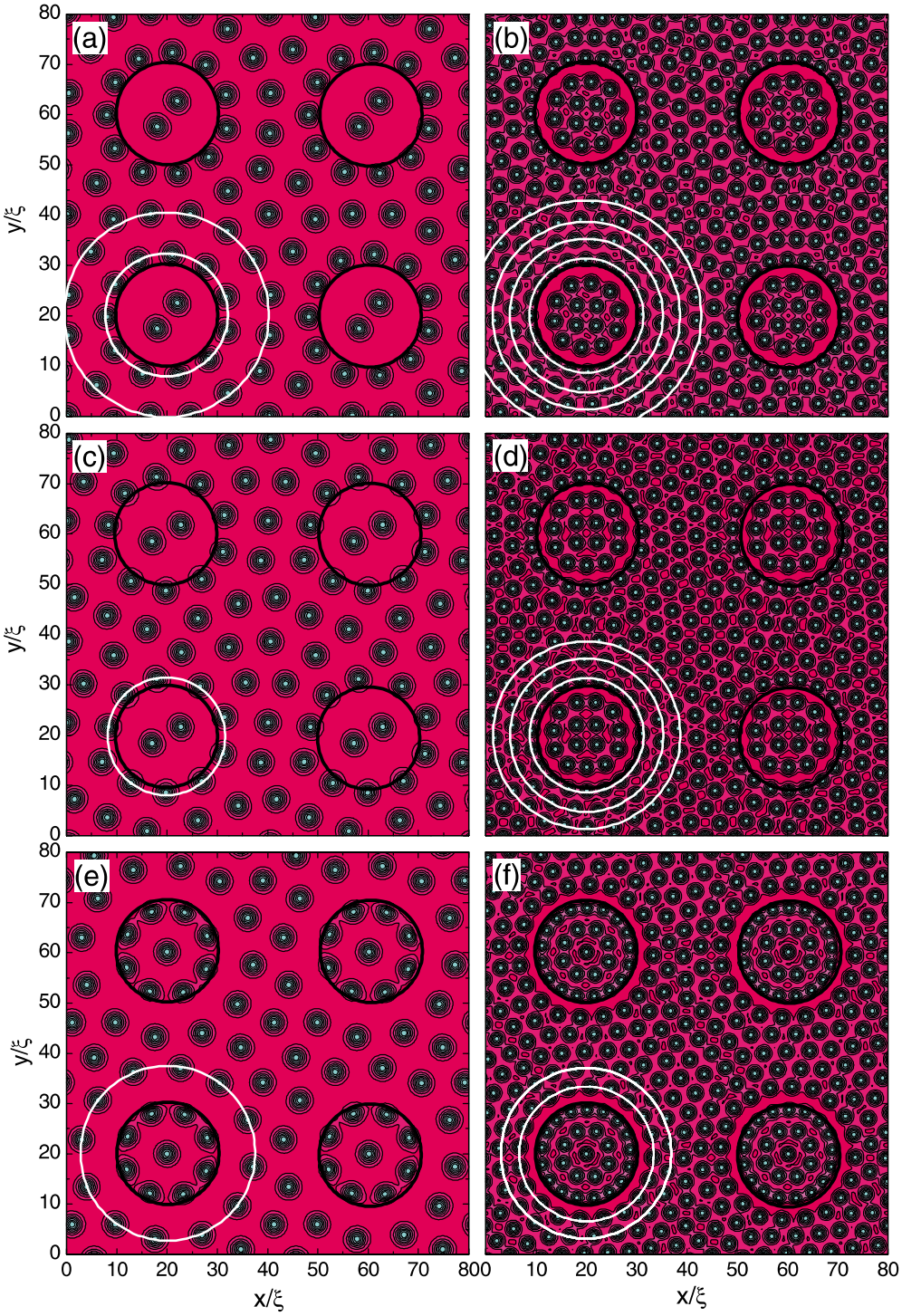

FIG. 9. (Color online) The vortex structure in a superconducting film of thickness $d=0.1\xi$ with arrays of pillars of radius $R=10\xi$ and period $W=30\xi$, for different thicknesses of the pillars: $d_i=0.5\xi$ [(a) and (b)] $d_i=0.2\xi$ [(c) and (d)] at the applied fields $H=H_{25}$ (left column) and $H=H_{100}$ (right column). (e) and (f) correspond to the case of blind holes with bottom thickness $d_i=0.01\xi$.

their top surfaces. In particular, the experiments confirmed that interstitial vortices closest to the pillars form circular shells very similar to those in Fig. 9. For sufficiently large R, the vortices inside the pillars also form circular shells as in Figs. 7 and 9, although the latter are somewhat distorted by pinning as discussed below. The pillars were prepared on the top surface of 0.5 mm thick Nb crystals by e-beam lithography and reactive etching (CF_4 with added oxygen). This was followed by high-vacuum annealing (at $<10^{-8}$ torr) at temperatures $\approx$750 °C in order to remove gaseous contaminants (primarily dissolved oxygen). The pillars have a range of heights between 0.5 and 1.4 μm and diameters between 0.4 and 2.0 μm. Vortex configurations were visualized using Bitter decoration technique after field cooling to $T\approx 2.5$K in perpendicular magnetic fields ranging from 30 to 100 Oe. For the decoration details, we refer to Refs. 9 and 10.

We note that the dimensions of the experimental system differ considerably from the theoretically studied samples, in particular, the radii of the pillars and the thickness of both the pillars and the base "film" are much greater than those in the simulations. Nevertheless, as was shown previously[9,10,22] vortex configurations in mesoscopic samples are determined

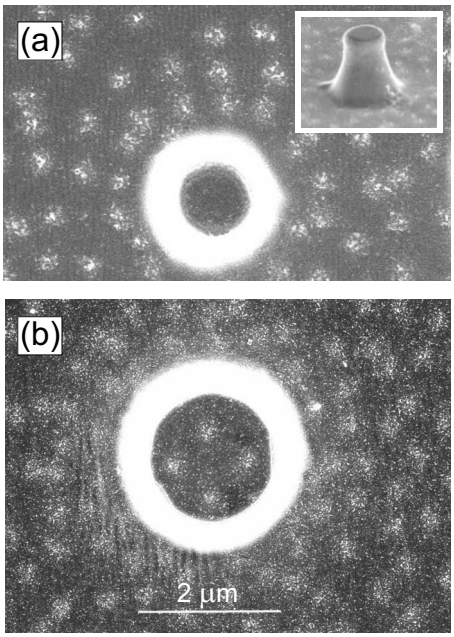

FIG. 10. Different snapshots of the vortex structure in a Nb sample with pillars of radii $R \approx 0.4$ μm (a) and $R \approx 0.8$ μm (b) decorated after field cooling in $H=50$ G. A three-dimensional image of a pillar with $R \approx 0.4$ μm is shown in the inset of (a).

predominantly by the total number of vortices (vorticity L) while depending only weakly on the absolute size of the sample. In addition, it was found[27] that the number of vortices and vortex configurations inside isolated pillars are independent of the pillars' height, at least for the heights between 0.5 and 1.5 μm, in agreement with Ref. 5. We therefore believe that, despite the above differences and the presence of pinning (that can be taken into account in the simulations -see below), comparison between the theory and experiment remains valid and indeed confirms main qualitative features discussed in the previous sections.

Figure 10(a) shows a typical vortex configuration in the Nb sample with pillars of radius $R \sim 0.4$ μm and height $h = 1.5$ μm. Because of the small size of the pillars and the small applied magnetic field ($H=50$ G) no vortices are present in the pillars. In terms of the field and/or pillar diameter combination, the vortex structures in Fig. 10 are closest to the numerical results shown in Figs. 8, 9(a), and 9(b) where we found that vortices nearest to each pillar form circular shells with a higher vortex density than that of the interstitial vortices further away from the pillars. Note that a thick bright circle around each pillar corresponds to the projection of the pillar wall, as for most pillars higher than ~ 0.5 μm the walls are not strictly vertical [see inset in Fig. 10(a)]. The arrangement of vortices away from the pillars is far from a perfect triangular Abrikosov vortex lattice which is related to the presence of *weak pinning* arising from gaseous contamination during lithography.[10] Despite the presence of disorder, there is clear evidence of such shells around the pillars in Fig. 10. Compared to the theory, the shells appear to be further away from the edge of the pillars which can be related to the complicated shape of the pillar walls [see inset in Fig. 10(a)] but should also be expected because of the much greater height to radius ratio d_i/R in the experiment (~ 3 compared to 0.01–0.05 in numerical simulations within the GL theory): as shown in Sec. III, higher pillars impose stronger repulsion on the surrounding vortices. Figure 10(a) zooms on the vortex shells around the pillars (although distorted due to the impurities) as discussed in the previous sections. With further increasing the radius of the pillars vortices start to penetrate the pillars, as shown in Fig. 10(b).

In the case of our largest pillars, i.e., $R \sim 2.0$ μm, vortices penetrate the pillars and arrange themselves in shells very similar to those shown in Fig. 7, although in experiment the shells are somewhat *distorted*, most likely due to *pinning* [see Fig. 11(a) where the vortex configuration inside the pillar corresponds to the state (1,5,11) with a shift toward the pillar edge]. For a more meaningful comparison between theory and experiment, it is necessary to include the effect of *weak disorder* on the vortex pattens in and around the pillars. To this end, we simulated vortex patterns in pillars in the presence of weak pinning using the Langevin molecular dynamics, following the approach developed in Ref. 22 for thick (macroscopic) disks (note that the samples with pillars we used in the experiment have thickness much larger than the penetration depth λ). Therefore we modified the model used in Ref. 22 to the case of large-radius pillars with radius $R > \lambda$ and height $h > \lambda$ which are placed on top of a film which is also thick ($d > \lambda$).

B. Molecular dynamics simulation of vortex shells in the presence of weak pinning

We also perform molecular dynamics simulations of vortex patterns inside and outside pillars taking into account the effect of weak random pinning. We used simulated annealing method integrating the overdamped equations of motion (see, e.g., Refs. 28–31—note, however, that here we study the relaxation of initially randomly distributed vortices to the ground-state vortex configuration, i.e., contrary to those papers we do not study the externally driven vortex dynamics and thus there is no driving force in our simulations; instead, we have additional contributions due to the interaction of vortices with the pillar boundaries) as follows

$$\eta \mathbf{v}_i = \mathbf{f}_i = \mathbf{f}_i^{vv} + \mathbf{f}_i^{vp} + \mathbf{f}_i^{vb} + \mathbf{f}_i^{v\text{-}pillar} + \mathbf{f}_i^{T}. \tag{7}$$

Here, $\mathbf{f}_i$ is the total force per unit length acting on vortex i, $\mathbf{f}_i^{vv}$ and $\mathbf{f}_i^{vp}$ are the forces due to vortex-vortex and vortex-pin interactions, respectively, $\mathbf{f}_i^{vb}$ is the force due to interaction of vortices inside the pillar with its boundary,[22] and $\mathbf{f}_i^{v\text{-}pillar}$ is the force of the repulsive interaction of vortices outside the pillar with its boundary [similarly to $\mathbf{f}_i^{vb}$, this force decays as $\exp(-r/\lambda)$ with distance from the pillar and will be discussed in detail in a separate paper[32]]. In Eq. (7), η is the viscosity, which is set here to unity. Vortices are excited by the thermal stochastic force $\mathbf{f}_i^T$. The force due to the interaction of the ith vortex with other vortices is

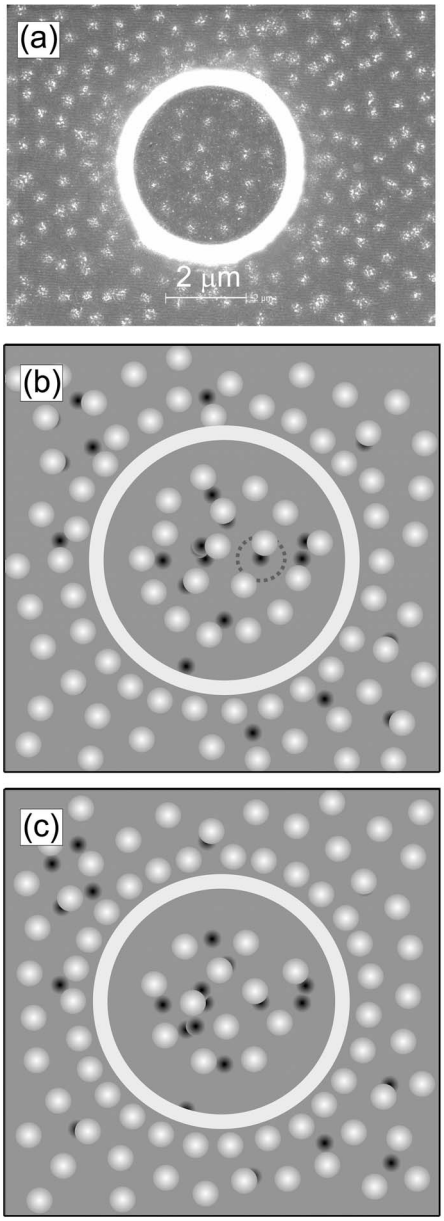

FIG. 11. Vortex patterns in large Nb pillars with radii $R=2.5$ μm [(a) and (b)] and $R=2.35$ μm (c) in the presence of weak pinning: (a) the experimental snapshot using the Bitter decoration technique, and [(b) and (c)] the calculated vortex pattern using molecular dynamics simulations. In panels (b) and (c), vortices are shown by light gray spots, while smaller dark gray spots show randomly distributed weak pinning sites with the pinning strength $f_p/f_0=0.2$. The radius of action of the pinning sites is shown by a dark gray dotted line in panel (b).

$$\mathbf{f}_i^{vv} = \sum_{j\neq i}^{N_v} f_0 K_1\left(\frac{|\mathbf{r}_i-\mathbf{r}_j|}{\lambda}\right)\hat{\mathbf{r}}_{ij}, \tag{8}$$

where N_v is the number of vortices, K_1 is the modified Bessel function, $\hat{\mathbf{r}}_{ij}=(\mathbf{r}_i-\mathbf{r}_j)/|\mathbf{r}_i-\mathbf{r}_j|$, and $f_0=\Phi_0^2/8\pi^2\lambda^3$. Following the notation used in Refs. 22 and 28–31, we express all the lengths in units of λ and all the fields in units of Φ_0/λ^2. The Bessel function $K_1(r)$ decays exponentially for r larger than λ; therefore, it is safe to cut off the (negligible) force for distances larger than 5λ. In our calculations, the logarithmic divergence of the vortex-vortex interaction forces for $r\to 0$ is eliminated by using a cutoff for distances smaller than 0.1λ.

We model weak pinning in a Nb film with pillars by placing randomly distributed weak pinning sites. Taken pinning force is

$$\mathbf{f}_i^{vp} = \sum_{k}^{N_p}\left(\frac{f_p}{r_p}\right)|\mathbf{r}_i-\mathbf{r}_k^{(p)}|\Theta(r_p-|\mathbf{r}_i-\mathbf{r}_k^{(p)}|)\hat{\mathbf{r}}_{ik}^{(p)}, \tag{9}$$

where N_p is the number of pinning sites, f_p is the maximal pinning force of each potential well, r_p is the spatial range of the pinning potential, Θ is the Heaviside step function, and $\hat{\mathbf{r}}_{ik}^{(p)}=(\mathbf{r}_i-\mathbf{r}_k^{(p)})/|\mathbf{r}_i-\mathbf{r}_k^{(p)}|$.

The temperature contribution to Eq. (7) is represented by a stochastic term obeying the following conditions:

$$\langle f_i^T(t)\rangle = 0 \tag{10}$$

and

$$\langle f_i^T(t)f_j^T(t')\rangle = 2\eta k_B T\delta_{ij}\delta(t-t'). \tag{11}$$

The ground state of a system of vortices is obtained as follows. First, we set a high value for the temperature, to let vortices move randomly. Then, the temperature is gradually decreased down to $T=0$. When cooled down, vortices interact with each other and with the edges, and arrange themselves to minimize the energy, essentially simulating the field-cooled experiments (see, e.g., Ref. 1).

The results for the pillars with $R=2.5$ μm and $R=2.35$ μm are shown in Figs. 11(b) and 11(c). One can see that the changes in vortex patterns brought about by pinning can consistently account for the differences between the experimentally observed vortex configurations [Figs. 10(b) and 11(a)] and those found numerically in the absence of pinning (cf. Figs. 7 and 9). Inside the pillars, vortices tend to form symmetric shell patterns, e.g., a three-shell pattern for $R=2.5$ μm in Fig. 11(b) (the "inner shell" consists of one vortex) due to the vortex-vortex interaction and the interaction with the edge of the pillar. The vortex pattern in this case is clearly affected by the random pinning (cf. vortex shell configurations for the pinning-free case in Fig. 7) but is still rather highly ordered because inside the pillar the vortex-pin interaction (which leads to disorder) competes with two other interactions which favor ordering, i.e., the vortex-vortex interaction and the interaction with circular pillar boundaries. In contrast, outside the pillars the effect of pinning is relatively stronger because the vortex-vortex interaction alone is not sufficiently strong to impose ordering into the Abrikosov lattice. A slightly smaller pillar with $R=2.35$ μm traps fewer vortices which can even form a square-lattice pattern [Fig. 11(c)] as sometimes observed in experiment.[9] Note that in the case of a much stronger pinning (we do not consider this regime here) the situation changes dramatically, and the presence of a strong pinning and disorder can even lead to the formation of vortex clusters and giant vortices.[10]

VI. CONCLUSIONS

We studied stable vortex configurations in a superconducting thin film with a square array of pillars in the framework of the GL theory. Our calculations show that numerous kinds of vortex lattice structures can be stabilized, some of which have different symmetries from the pillar lattice. For example, for small radius of the pillars triangular vortex lattice still exists and with increasing the radius of the pillars it gradually transforms into a square vortex lattice. In the intermediate cases vortex chain structures may be formed as well as clusters of vortex molecules at the interstitial sites, depending on the applied magnetic field. For larger density of vortices, clusters are particularly favorable around the pillars. To illustrate the transition between these vortex states we constructed a structural phase diagram, as a function of the radius of the pillars and interpillar distance for different thicknesses of pillars. For larger radius of the pillars vortices start to penetrate them, overcoming the Bean-Livingston energy barrier at the pillar boundaries. With increasing the density of vortices, the vortex shell structures are formed in the pillars, similar to the ones characteristic for superconducting disks. When the pillars are far apart, the shell structures inside them are actually almost identical to those in individual disks. However, if the pillars are placed closer together, the vortex patterns inside depend on pillar size, density, and the arrangement of interstitial vortices. Due to the influence of these shell structures, as well as due to the boundaries of the pillars, a transition from Abrikosov-like vortex lattice to vortex shell structures takes place at the interstitial sites.

The presence of vortex shell structures inside and around the pillars etched in the surface of thin Nb platelets was shown experimentally using the Bitter decoration technique. In addition, we show that the predicted vortex states and transition between them can be obtained using local magnetization measurements, such as Hall probe measurements. The magnetization shows clear hysteresis which arises from the difference in the topology of the vortex states during the heating and cooling processes. We also considered the effect of weak pinning in the superconductor on the vortex shell formation process using molecular dynamics simulations. The obtained results agree qualitatively with the observed distortion of the vortex shells in the presence of weak pinning.

ACKNOWLEDGMENTS

This work was supported by the Flemish Science Foundation (FWO-Vl), the Interuniversity Attraction Poles (IAP) Programme-Belgian State-Belgian Science Policy, and the ESF-AQDJJ network. V.R.M. and M.V.M. acknowledge support from the EU Marie Curie Incoming-International and Intra-European programs. G.R.B acknowledges support from FWO-Vlaanderen.

*francois.peeters@ua.ac.be

[1] K. Harada, O. Kamimura, H. Kasai, T. Matsuda, A. Tonomura, and V. V. Moshchalkov, Science **274**, 1167 (1996).
[2] V. V. Moshchalkov, M. Baert, V. V. Metlushko, E. Rosseel, M. J. Van Bael, K. Temst, R. Jonckheere, and Y. Bruynseraede, Phys. Rev. B **54**, 7385 (1996).
[3] V. Metlushko, U. Welp, G. W. Crabtree, R. Osgood, S. D. Bader, L. E. DeLong, Zhao Zhang, S. R. J. Brueck, B. Ilic, K. Chung, and P. J. Hesketh, Phys. Rev. B **60**, R12585 (1999).
[4] G. R. Berdiyorov, M. V. Milošević, and F. M. Peeters, Phys. Rev. Lett. **96**, 207001 (2006); Phys. Rev. B **74**, 174512 (2006).
[5] A. Bezryadin, Yu. N. Ovchinnikov, and B. Pannetier, Phys. Rev. B **53**, 8553 (1996).
[6] S. Raedts, A. V. Silhanek, M. J. Van Bael, and V. V. Moshchalkov, Phys. Rev. B **70**, 024509 (2004).
[7] M. Lange, M. J. Van Bael, Y. Bruynseraede, and V. V. Moshchalkov, Phys. Rev. Lett. **90**, 197006 (2003); M. V. Milošević and F. M. Peeters, Europhys. Lett. **70**, 670 (2005).
[8] M. V. Milošević, S. V. Yampolskii, and F. M. Peeters, Phys. Rev. B **66**, 174519 (2002); M. V. Milošević and F. M. Peeters, *ibid.* **68**, 094510 (2003).
[9] I. V. Grigorieva, W. Escoffier, J. Richardson, L. Y. Vinnikov, S. Dubonos, and V. Oboznov, Phys. Rev. Lett. **96**, 077005 (2006).
[10] I. V. Grigorieva, W. Escoffier, V. R. Misko, B. J. Baelus, F. M. Peeters, L. Y. Vinnikov, and S. V. Dubonos, Phys. Rev. Lett. **99**, 147003 (2007).
[11] G. R. Berdiyorov, M. V. Milošević, B. J. Baelus, and F. M. Peeters, Phys. Rev. B **70**, 024508 (2004).
[12] V. A. Schweigert, F. M. Peeters, and P. S. Deo, Phys. Rev. Lett. **81**, 2783 (1998); V. A. Schweigert and F. M. Peeters, Phys. Rev. B **57**, 13817 (1998).
[13] R. Kato, Y. Enomoto, and S. Maekawa, Phys. Rev. B **47**, 8016 (1993).
[14] M. M. Doria, J. E. Gubernatis, and D. Rainer, Phys. Rev. B **39**, 9573 (1989).
[15] G. Karapetrov, J. Fedor, M. Iavarone, D. Rosenmann, and W. K. Kwok, Phys. Rev. Lett. **95**, 167002 (2005).
[16] A. Oral, S. J. Bending, and M. Henini, Appl. Phys. Lett. **69**, 1324 (1996).
[17] T. Nishizaki, Y. Onodera, N. Kobayashi, H. Asaoka, and H. Takei, Phys. Rev. B **53**, 82 (1996).
[18] C. Reichhardt and N. Gronbech-Jensen, Phys. Rev. B **63**, 054510 (2001).
[19] C. Reichhardt and C. J. Olson, Phys. Rev. Lett. **88**, 248301 (2002).
[20] Yu. E. Lozovik and E. A. Rakoch, Phys. Rev. B **57**, 1214 (1998).
[21] B. J. Baelus, L. R. E. Cabral, and F. M. Peeters, Phys. Rev. B **69**, 064506 (2004).
[22] V. R. Misko, B. Xu, and F. M. Peeters, Phys. Rev. B **76**, 024516 (2007).
[23] L. R. E. Cabral, B. J. Baelus, and F. M. Peeters, Phys. Rev. B **70**, 144523 (2004).
[24] G. R. Berdiyorov, L. R. E. Cabral, and F. M. Peeters, J. Math. Phys. **46**, 095105 (2005).
[25] A. K. Geim, I. V. Grigorieva, S. V. Dubonos, J. G. S. Lok, J. C. Maan, A. E. Filipov, and F. M. Peeters, Nature (London) **390**,

259 (1997); A. K. Geim, S. V. Dubonos, J. G. S. Lok, M. Henini, and J. C. Maan, *ibid.* **396**, 144 (1998).
[26] V. M. Bedanov and F. M. Peeters, Phys. Rev. B **49**, 2667 (1994).
[27] I. V. Grigorieva (unpublished).
[28] F. Nori, Science **278**, 1373 (1996); C. Reichhardt, C. J. Olson, J. Groth, S. Field, and F. Nori, Phys. Rev. B **52**, 10441 (1995); **53**, R8898 (1996); C. Reichhardt, C. J. Olson, J. Groth, S. Field, and F. Nori, *ibid.* **54**, 16108 (1996); **56**, 14196 (1997).
[29] C. Reichhardt, C. J. Olson, and F. Nori, Phys. Rev. B **57**, 7937 (1998).
[30] C. Reichhardt, C. J. Olson, and F. Nori, Phys. Rev. Lett. **78**, 2648 (1997); Phys. Rev. B **58**, 6534 (1998).
[31] V. R. Misko, S. Savel'ev, and F. Nori, Phys. Rev. Lett. **95**, 177007 (2005); Phys. Rev. B **74**, 024522 (2006).
[32] V. R. Misko, G. R. Berdiyorov, and F. M. Peeters (unpublished).